

Numerical and physical instability of subglacial water flow

K. L. P. Warburton, C. R. Meyer, A. N. Sommers

@kasiawarburton, @colinmeyer,

Thayer School of Engineering, Dartmouth College, Hanover, NH 03755, USA

@thayerschool

This paper is a non-peer reviewed preprint submitted to EarthArXiv, that has also been submitted to JGR: Earth Surface

Numerical and physical instability of subglacial water flow

K. L. P. Warburton¹, C. R. Meyer¹, A. N. Sommers¹

¹Thayer School of Engineering, Dartmouth College, Hanover, NH 03755, USA

Key Points:

- We perform a linear stability analysis of subglacial water flow across different scales of perturbation to explain the onset of channels
- Channels develop under glaciers when the meltwater input exceeds a threshold dependent on ice thickness and geothermal flux
- Lateral heat transport must be included in numerical models to resolve channel geometry

Corresponding author: Kasia Warburton, kasia.warburton@dartmouth.edu

Abstract

The sliding speed of glaciers depends strongly on the water pressure at the ice-sediment interface, which is controlled by the efficiency of water transport through a subglacial hydrological system. The least efficient component of the system is a ‘distributed’ uniform sheet flow everywhere beneath the ice, whereas the ‘channelised’ drainage through large, thermally eroded conduits is more efficient. To understand the conditions under which the subglacial network channelises, we perform a linear stability analysis of distributed flow, considering competition between thermal erosion and viscous ice collapse. We derive a stability criterion and determine the minimum subglacial meltwater flux needed for channels to form. We demonstrate the need to include lateral heat diffusion when modeling melt incision to resolve channel widths. We also show that low numerical resolution can suppress channel formation and lead to overestimates of water pressure. We demonstrate the applicability of linear stability results to predicting the character of subglacial hydrological networks without recourse to numerical modeling.

Plain Language Summary

Meltwater underneath glaciers causes the ice to slide faster. During summer months, when there is a lot of water present, heat produced by the water flow can melt large channels into the base of the ice. These channels efficiently drain water out from the bed of the glacier, slowing down the ice flow. We study when and where channels are likely to form by considering whether local increases in water depth grow larger via positive feedback loops, or shrink away. We show our criterion for when channels form matches the results of numerical simulations but is much faster to calculate. This could be used to rapidly predict drainage beneath and seasonal patterns of speed of different glaciers, and how these will evolve under warming conditions.

1 Introduction

The Greenland Ice Sheet is the current largest contributor to sea-level rise due to widespread thinning and melting of the ice (Mouginot et al., 2019; Otosaka et al., 2023). Greenland’s glaciers transport ice from the interior of the ice sheet to the ablation zone around the margin. The speed of ice flow is in large part due to sliding at the bed (Rignot & Mouginot, 2012; MacGregor et al., 2016; Maier et al., 2019), the rate of which depends strongly on the effective pressure, defined as the difference between the pressure exerted by the overlying ice and the water pressure, $N = p_i - p_w$ (e.g. Schoof, 2005; Helanow et al., 2021; Schoof, 2023; Warburton et al., 2023). Thus, understanding the future of the Greenland Ice Sheet requires an understanding of the way subglacial water pressure evolves in time, over a melt-season and over several decades (Nienow et al., 2017; Aschwanden et al., 2019).

Subglacial hydrological networks span a continuum from inefficient, distributed flow through connected cavities and sediment layers, to channelised, efficient drainage pathways through meltwater channels (Schoof, 2010). The transition between distributed and channelised drainage is thought to play a large role in the seasonal patterns of ice sheet velocity across Greenland (Bartholomew et al., 2011; I. J. Hewitt, 2013) and during glacier surges. For a given volume of surface meltwater passing through the subglacial hydrology, distributed systems will show higher inland water pressure p_w , lower effective pressure, lower basal friction, and faster flow speeds as compared to the channelised network. Throughout a melt season, basal water pressure generally increases, leading to faster glacier flow (Zwally et al., 2002), until in some cases channelization initiates, the bed drains, and the ice slows (I. J. Hewitt, 2013).

Depending on whether the summertime velocities are above or below the winter average, Greenland outlet glaciers can be categorised by type (Moon et al., 2014; Vijay

61 et al., 2021; Poinar, 2023). This categorisation shows some spatial clustering of seasonal
62 patterns, but also reveals that the response of a single glacier can change year-on-year
63 based on the climatic conditions, and neighbouring glaciers can respond quite differently.
64 Models of summertime hydrology often assume that no channels persist through the win-
65 ter, but some studies show persistent winter channels (Hager et al., 2022; Sommers et
66 al., 2023). Thus a small velocity response could be attributable either to no channeliza-
67 tion during the summer or persistent channelization during the winter. Understanding
68 the drivers of current seasonal velocity trends, by predicting when glaciers have chan-
69 nelled subglacial networks, would give better constraints on their future evolution in a
70 changing climate. Models of future ice sheet evolution generally rely on current estimates
71 of basal slipperiness, which is strongly affected by basal effective pressure and therefore
72 by subglacial channelization (e.g. Morlighem et al., 2010; Seroussi et al., 2013; Shapero
73 et al., 2016).

74 Direct observations of subglacial channels, particularly of their spatial patterning
75 and evolution over a melt-season, are limited (e.g. Andrews et al., 2014; Rada & Schoof,
76 2018). The question of which glaciers have subglacial channels is therefore often left purely
77 to numerical models of the hydrology. However, given the number of such models (c.f.
78 Flowers, 2015), and the differing choices in their modelled processes and parametriza-
79 tions (e.g. Brinkerhoff et al., 2021), the question persists: what balances govern the in-
80 stability of distributed water flow and its tendency to channelise, to what extent are these
81 model-dependent (c.f. de Fleurian et al., 2018), resolution dependent, versus robust phys-
82 ical properties expected of the flow.

83 Walder (1982), in an early study of subglacial water flow, noted the tendency of
84 sheet (distributed) flow to go unstable in ways that rapidly become unphysical, with thicker
85 regions of the sheet able to generate more dissipative heating and melt into the ice above.
86 Beyond this linear instability, nonlinear features such as channels must form (Schoof, 2010).
87 To study this in numerical simulations, many models (c.f. Flowers, 2015) employ sep-
88 arate equations for the distributed and channelised flow, turning off dissipative heating
89 in the distributed regions, and in certain cases (e.g. Werder et al., 2013) a priori impos-
90 ing potential locations for the channels.

91 In SHAKTI (Sommers et al., 2018), a single laminar-to-turbulent transitional water-
92 flow model is imposed throughout the domain, and all components of the melt rate are
93 included everywhere. This allows channel-like features to appear at self-determined lo-
94 cations anywhere in the domain. However, despite the ability of the model to produce
95 channel-like features, these features are always one grid point wide, indicating a collapse
96 to the smallest scales, limited only by resolution of the simulation. Further, the spac-
97 ing, inland extent, and in some cases the appearance of channels itself all depend on the
98 grid size chosen, similar to features noted in models of marine ice sheets (Cornford et
99 al., 2016).

100 This tendency towards an infinite narrowing of unstable features, referred to in the
101 context of classical stability analysis as an ‘ultraviolet catastrophe’, is, as described by
102 I. J. Hewitt (2011), indicative of an ill-posed mathematical model for the system, in which
103 the shortest wavelengths are the most unstable, a sign that a process neglected in the
104 model should become important. In his thesis, I. J. Hewitt (2009) derived a maximum
105 growth rate for distributed flow and provided a physical argument that such a break-
106 down ought to occur given the model components. We also see the ultraviolet catastro-
107 phe in the non-convergence of the SHAKTI equations when implemented in adaptive mesh
108 schemes (Felden et al., 2023), in which the channels continue to narrow towards infinitely
109 small scales. In contrast, a well-posed model should display wavelength selection, where
110 a perturbation with intermediate wavelength produces the highest growth rate. Felden
111 et al. (2023) regularised their model by introducing a numerically-motivated diffusion-
112 like term and found this produced convergent channel widths.

113 In this paper, we begin by completing the linear stability analysis of distributed
 114 flow, reviewing the stability criterion of I. J. Hewitt (2009), and confirming the existence
 115 of the short-wavelength blow-up. We also use this to explore the stability of long-wavelength
 116 features, and show how this could lead low-resolution simulations to numerically sup-
 117 press channel formation. We then revisit the origin of the melt-rate equation and locate
 118 a missing diffusion-like term, which is similar though not identical to the form posited
 119 in Felden et al. (2023). We find that this term, which we show comes from lateral dif-
 120 fusion of heat, regularises the stability analysis and allows for wavelength selection, in-
 121 dicating that we have found a well-posed model of the system. In the final section of the
 122 paper, we implement our new set of equations in an adaptive mesh scheme, and demon-
 123 strate that our linear stability analysis predicts the model results without need for sim-
 124 ulation. We show that channel onset is predicted by our stability criterion, and end by
 125 discussing the applicability of this work to predicting seasonal trends in subglacial hy-
 126 drology.

127 2 Linear stability of distributed flow

128 2.1 Full model equations

129 In this work, we take as our governing equations those of SHAKTI (Sommers et
 130 al., 2018), but, by design, our results are largely independent of the exact formulation.
 131 The main difference between SHAKTI and other models of subglacial flow is the form
 132 of the power-law relating the flux, water depth, and pressure gradients (see Appendix
 133 A). That choice can be changed in the following analysis with only a quantitative, not
 134 qualitative difference to the results.

135 We consider a water-filled space between the ice and bed with effective gap-height
 136 b (figure 1), through which flows a flux of meltwater \mathbf{q} . If the rate at which melt erodes
 137 the water-ice interface over a given area is \dot{m} , then conservation of mass in the fluid layer,
 138 balancing changes in gap height with lateral flow of meltwater and local water sources,
 139 is given by

$$\frac{\partial b}{\partial t} + \nabla \cdot \mathbf{q} = \frac{\dot{m}}{\rho_w} + i_{eb}, \quad (1)$$

140 where ρ_w is the density of water (so \dot{m}/ρ_w is the volume of water produced by basal melt)
 141 and i_{eb} is the rate at which surface meltwater is delivered to the bed.

142 Tracking the vertical motion of the ice-water interface due to melting upwards, the
 143 downwards viscous collapse of the overlying ice, and opening by sliding over bumps, we
 144 have

$$\frac{\partial b}{\partial t} = \frac{\dot{m}}{\rho_i} - AN^n b + \frac{(b_r - b)u_b}{l_r}, \quad (2)$$

145 where ρ_i is the density of ice (so \dot{m}/ρ_i is the volume of ice removed by melt), u_b is the
 146 sliding speed, b_r is the characteristic height of bumps, and l_r the bump spacing. The col-
 147 lapse term is controlled by A , the viscosity parameter for the ice, with a power-law ex-
 148 ponent n , and N is the effective pressure, the difference between the ice overburden and
 149 the water pressure, $N = p_i - p_w$. In equation (2), we take the closure lengthscale (av-
 150 erage cavity width) as equal to b (Schoof, 2010; Werder et al., 2013; Sommers et al., 2018),
 151 but other functions of b have also been proposed, such as $l_r/(1-b/b_r)$ by Kyrke-Smith
 152 et al. (2014). Because opening by sliding may be less active beneath soft-bedded glaciers
 153 (Sommers et al., 2023), we include it in our analysis for comparison with I. J. Hewitt (2011),
 154 but remove it in our example calculations.

155 We take the flux through the water layer, driven by gradients in the pressure head
 156 $h = p_w/\rho_w g + z_b$, where z_b is the bed elevation, to be given by a modified Poiseuille
 157 flow,

$$\mathbf{q} = -\frac{b^3 g}{12\nu(1 + \omega Re)} \nabla h, \quad (3)$$

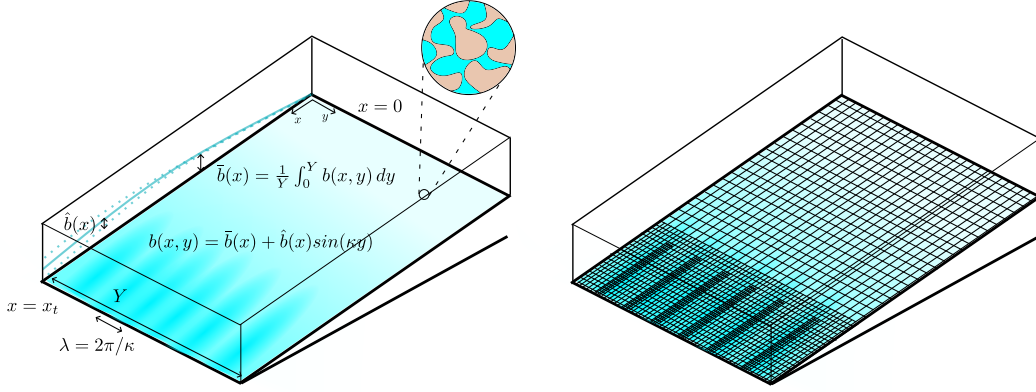


Figure 1. Left, the geometry used in this paper, showing the ice divide at $x = 0$, the terminus as x_t , and an example gap height distribution $b(x, y)$ (color), with width-average $\bar{b}(x)$ and variation of size $\hat{b}(x)$ at a wavelength λ . The spatial structure of pressure head and flux is similarly decomposed into an average plus a periodic perturbation. Away from channels, the effective gap height b represents a local average over flow through connected cavities (inset). Right, a schematic showing mesh refinement in the numerical simulations, with finer meshes in areas of higher spatial variability. Each step in refinement halves the grid size. Both the minimum and maximum levels of refinement can be set manually and we use up to 10 levels (compared to the 3 shown here). Only perturbations where λ is at least twice the minimum grid size can be resolved numerically.

158 where ν is the water viscosity, ω is a parameter setting transition between laminar flow
 159 and a turbulent, Darcy-Weisbach flow law, where $Re = q/\nu$ is the Reynolds number
 160 determining the flow character. There are other possible formulations of this transition
 161 to turbulence (e.g. D. R. Hewitt et al., 2018), and we take this expression for consistency
 162 with prior work (Sommers et al., 2018; Zimmerman et al., 2004) and its simple form.

163 Finally, the melt rate is found by considering a vertical balance of heat fluxes, so
 164 that

$$\dot{m} = \frac{1}{L} (G + |\mathbf{u}_b \cdot \boldsymbol{\tau}_b| - \rho_w g \mathbf{q} \cdot \nabla h), \quad (4)$$

165 where $\dot{m}L$ is the latent heat flux required to melt the ice, G is the geothermal flux, and
 166 $|\mathbf{u}_b \cdot \boldsymbol{\tau}_b|$ is the frictional heat flux produced by the sliding of the glacier over the bed,
 167 $-\rho_w g \mathbf{q} \cdot \nabla h$ is the dissipative heat flux produced by friction in the flow of water itself.
 168 In this work, we neglect the changes in melting temperature due to pressure variations,
 169 which would otherwise appear as a heat sink in (4). We assume a Budd-style friction of
 170 the form

$$\boldsymbol{\tau}_b = C^2 N \mathbf{u}_b, \quad (5)$$

171 where C is a friction coefficient, taken as uniform in our simulations. The dependence
 172 on the effective pressure N reflects that subglacial hydrology is a strong control on basal
 173 traction, although in this paper we do not account for the feedback of N on the sliding
 174 speed u_b , which we take as known (e.g. from satellite observations).

175 2.2 Steady background state

176 To begin our linear stability analysis, we calculate the laterally uniform, constant
 177 in time solution to our governing equations, representing the distributed system before

178 channels form. The growth rate of the linear perturbations will be determined by this
 179 background state.

180 This solution is given by the profiles of gap height, pressure head, and flux

$$b = \bar{b}(x), \quad h = \bar{h}(x), \quad q = \bar{q}(x), \quad (6)$$

181 from $x = 0$, the ice divide, to $x = x_t$, the terminus (figure 1), which solve the govern-
 182 ing equations (1-4) with all time-derivatives and y (lateral) variation ignored,

$$\frac{d\bar{q}}{dx} = \frac{\bar{m}}{\rho_w} + i_{eb}, \quad (7)$$

$$\frac{\bar{m}}{\rho_i} = A\bar{N}^n\bar{b} - \frac{(b_r - \bar{b})u_b}{l_r}, \quad (8)$$

$$\bar{q} = -\frac{\bar{b}^3 g}{12\nu(1 + \omega Re)} \frac{d\bar{h}}{dx}, \quad (9)$$

$$\bar{m} = \frac{1}{L} \left(G + |\mathbf{u}_b \cdot \boldsymbol{\tau}_b| - \rho_w g \bar{q} \frac{d\bar{h}}{dx} \right). \quad (10)$$

183 The ice thickness H (and hence ice overburden pressure $p_i = \rho_i g H$), the bed topog-
 184 raphy z_b , and the surface meltwater input i_{eb} that drive the subglacial hydrology need
 185 to be imposed throughout the modelled domain, and for the purposes of stability anal-
 186 ysis, are also assumed to be only functions of distance from the terminus.

187 The boundary conditions are atmospheric pressure $\bar{p}_w(x_t) = 0$ at the terminus,
 188 and zero meltwater flux $\bar{q}(0) = 0$ at the divide. With one boundary condition at each
 189 end of the domain, we solve these equations using a shooting method: integrating from
 190 the terminus towards the divide, starting with the correct imposed water pressure at the
 191 terminus and a guess of the outflow flux $\bar{q}(x_t)$, then use a root-finding algorithm to re-
 192 fine the outflow until there is no flux at the ice divide, $\bar{q}(0) = 0$.

193 An example solution is shown in figure 2 for constant ice thickness, basal slope, and
 194 surface meltwater input (values of parameters given in caption). In this example, the sub-
 195 glacial water flux \bar{q} increases nearly linearly towards the terminus, fed by the constant
 196 input of meltwater from the surface, leading to a high pressure head \bar{h} in the interior that
 197 decreases rapidly towards the terminus. The gap height \bar{b} initially increases to accom-
 198 modate the additional meltwater, but drops towards the terminus due to the increased
 199 rate of viscous ice collapse as the effective pressure \bar{N} increases.

200 2.3 Normal mode perturbations

201 With these background conditions established, we now introduce small periodic per-
 202 turbations on top of the background state and calculate whether any wavelengths lead
 203 to perturbations that are expected to grow (leading to eventual channelization) or if in-
 204 stead disturbances decay back towards the distributed system found above.

205 Each possible cross-flow wavelength $\lambda = 2\pi/\kappa$ is associated with a growth rate
 206 $\sigma(\kappa)$ and an along-flow structure $\hat{b}(x)$, $\hat{h}(x)$ and $\hat{\mathbf{q}}(x)$, which describe how the pertur-
 207 bations evolve between the terminus and the ice divide (figure 1). The overall perturbed
 208 gap height, pressure head, and flux are given by

$$b = \bar{b}(x) + \hat{b}(x)e^{i\kappa y + \sigma t}, \quad (11)$$

$$h = \bar{h}(x) + \hat{h}(x)e^{i\kappa y + \sigma t}, \quad (12)$$

$$\mathbf{q} = \bar{\mathbf{q}}(x) + \hat{\mathbf{q}}(x)e^{i\kappa y + \sigma t}. \quad (13)$$

211 Substituting these expressions into the equation for the flux (3), and retaining only
 212 the terms linear in the perturbations, we find that the perturbed flux can be expressed

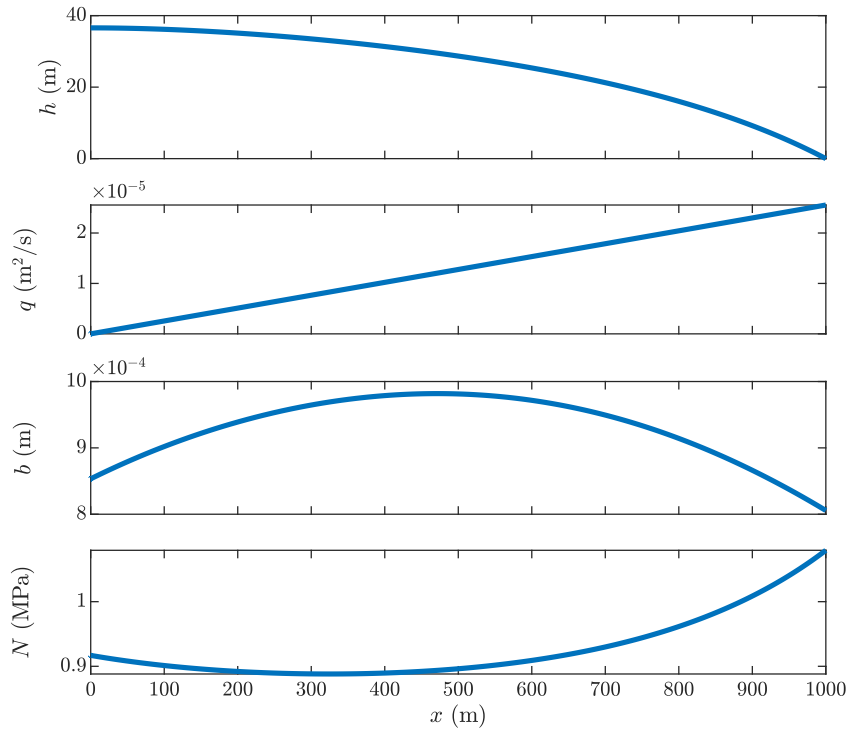


Figure 2. An example of the background solution for laterally uniform pressure head \bar{h} , water flux \bar{q} , gap height \bar{b} , and effective pressure \bar{N} solving (7-10) from the ice divide at $x = 0$ to the terminus at 1km, in the case of a constant ice thickness of 120m, distributed meltwater input of 0.8m/year, and a slope of 0.02 towards the terminus. Gap opening by sliding is ignored in all simulations.

Grouping	Definition	Interpretation
K	$\frac{\bar{b}^3 g}{12\nu(1+\omega \bar{q} /\nu)}$	Hydraulic transmissivity of distributed flow
Q_b	$\frac{3\bar{q}(1+\omega \bar{q} /\nu)}{\bar{b}(1+2\omega \bar{q} /\nu)}$	Speed of gap height advection
Q_h	$\frac{\bar{b}^3 g}{12\nu(1+2\omega \bar{q} /\nu)}$	Transmissivity of head perturbations
U	$\frac{\rho_w g u_b^2 \mu^2}{L}$	Sensitivity of frictional melt to pressure
M_b	$\frac{36\nu\rho_w \bar{q}^2 (1+\omega \bar{q} /\nu)^2}{\bar{b}^4 L (1+2\omega \bar{q} /\nu)}$	Sensitivity of melt-rate to gap height
M_h	$\frac{\rho_w g \bar{q} (2+3\omega \bar{q} /\nu)}{L (1+2\omega \bar{q} /\nu)}$	Sensitivity of melt-rate to pressure gradients

Table 1. Definitions of the functions of the background state used to streamline the stability analysis, and their physical interpretations.

213 in terms of the background state and the gap and pressure perturbations as

$$\hat{\mathbf{q}} = -\frac{\bar{b}^3 g}{12\nu(1+\omega|\bar{q}|/\nu)} \left[\frac{1+\omega|\bar{q}|/\nu}{(1+2\omega|\bar{q}|/\nu)} \left(\frac{3\hat{b}}{\bar{b}} \frac{d\bar{h}}{dx} + \frac{\partial\hat{h}}{\partial x} \right) \hat{\mathbf{x}} + \frac{\partial\hat{h}}{\partial y} \hat{\mathbf{y}} \right] \quad (14)$$

214 and the perturbation to the divergence in flux is therefore

$$\nabla \cdot \hat{\mathbf{q}} = \frac{\partial}{\partial x} \left[\frac{-\bar{b}^3 g}{12\nu(1+2\omega|\bar{q}|/\nu)} \left(\frac{3\hat{b}}{\bar{b}} \frac{d\bar{h}}{dx} + \frac{\partial\hat{h}}{\partial x} \right) \right] + \frac{\bar{b}^3 g \kappa^2}{12\nu(1+\omega|\bar{q}|/\nu)} \hat{h}. \quad (15)$$

215 For convenience in the following analysis, we give names to these functions of the base
216 state, and write

$$\nabla \cdot \hat{\mathbf{q}} = \frac{\partial}{\partial x} \left(Q_b \hat{b} - Q_h \frac{\partial\hat{h}}{\partial x} \right) + K \kappa^2 \hat{h}. \quad (16)$$

217 The functions $Q_b(x)$, $Q_h(x)$, and $K(x)$ are always positive, and describe how easily vari-
218 ations in pressure and gap height are transported in different regions of the distributed
219 system (see table 1).

220 Substituting the expression for the flux into the melt rate (4), we find that melt-
221 rate perturbations can also be expressed in terms of pressure head and gap height,

$$\hat{m} = \frac{\rho_w g}{L} \left(-u_b^2 \mu^2 \hat{h} - \frac{1+\omega|\bar{q}|/\nu}{1+2\omega|\bar{q}|/\nu} \bar{q} \frac{3}{\bar{b}} \frac{d\bar{h}}{dx} \hat{b} - \frac{2+3\omega|\bar{q}|/\nu}{1+2\omega|\bar{q}|/\nu} \bar{q} \frac{\partial\hat{h}}{\partial x} \right). \quad (17)$$

222 Again, we give names to these functions of the base state (table 1), so

$$\hat{m} = -U(x) \hat{h} + M_b(x) \hat{b} - M_h \frac{\partial\hat{h}}{\partial x}. \quad (18)$$

223 Here, $U(x)$ describes the impact of pressure variations on friction at the glacier bed, $M_b(x)$
224 describes how sensitive the melt-rate is to changes in gap height, and $M_h(x)$ describes
225 how changes in pressure gradients impact the melt-rate through changes in flow rate. Again,
226 all these functions are defined so as to be positive quantities (the sensitivity of melt rate
227 to the different variables). Turning off dissipative heating in the distributed system cor-
228 responds to a case where M_h and M_b are both zero, which we shall see immediately re-
229 moves the possibility of instability.

230 Inserting these results into the motion of the ice-water interface (2), we obtain a
231 first equation linking changes in water pressure to the growth rate of the gap height per-
232 turbation,

$$\left(\sigma - \frac{M_b}{\rho_i} + A\bar{N}^n + \frac{u_b}{l_r} \right) \hat{b} = \left(A n \bar{N}^{n-1} \rho_w g \bar{b} - \frac{U}{\rho_i} \right) \hat{h} - \frac{M_h}{\rho_i} \frac{\partial\hat{h}}{\partial x}. \quad (19)$$

233 Note that if there were no perturbation to the pressure head, i.e. $\hat{h}(x) = 0$, the growth
 234 rate would be given by a local, wavelength-independent competition between the ten-
 235 dency of larger gaps promote melt via accommodating faster, more dissipative flow, and
 236 their more rapid collapse, which we denote by

$$\sigma_0 = \frac{M_b}{\rho_i} - A\bar{N}^n - \frac{u_b}{l_r}. \quad (20)$$

237 The shape of $\sigma_0(x)$ for the example of figure 2 is shown in figure 3a, and in general is
 238 negative close to the ice divide, where M_b is small, but increases towards the terminus.

239 Meanwhile, the perturbation to conservation of mass (1) simplifies to

$$\sigma \hat{b} = -\frac{\partial}{\partial x} \left(Q_b \hat{b} - Q_h \frac{\partial \hat{h}}{\partial x} \right) - K \kappa^2 \hat{h} + \frac{M_b}{\rho_w} \hat{b} - \frac{U}{\rho_w} \hat{h} - \frac{M_h}{\rho_w} \frac{\partial \hat{h}}{\partial x}. \quad (21)$$

240 This equation describes how the larger, longer wavelength perturbations tend to be sta-
 241 bilised due to the large gradients in pressure head required to sustain flow into them (compare
 242 to the similar stabilisation by mass conservation noted in Brinkerhoff et al., 2016)

243 Together, the pair of differential equations for \hat{h} and \hat{b} (19, 21) at a particular value
 244 of κ has the structure of an eigenfunction problem, where the growth rate $\sigma(\kappa)$ is the
 245 eigenvalue, i.e. the only value of σ that allows all the boundary conditions to be simul-
 246 taneously met. The boundary conditions are $\hat{h}(0) = 0$ (no pressure variations at the
 247 terminus, as the outflow pressure is the same everywhere); the decay of \hat{h} and \hat{b} towards
 248 the ice divide (inspecting the structure of the differential equations, this turns out to be
 249 a single condition); and finally since both equations are linear and we can multiply both
 250 $\hat{b}(x)$ and $\hat{h}(x)$ by any constant value without affecting the structure of the solution, we
 251 impose $\hat{b}(0) = 1$ for convenience.

252 Solving for \hat{h} , \hat{b} , and σ as a function of κ is in general only possible numerically given
 253 the complex structure of the background state. To do so, for each value of κ , we guess
 254 a value of σ , begin with very small \hat{h} and \hat{b} close to the ice divide, then integrate the equa-
 255 tions forwards towards the terminus to find $\hat{h}(x_t)$. We then iterative update the value
 256 of σ until we find a value producing $\hat{h}(x_t) = 0$. These numerically calculated values of
 257 $\sigma(\kappa)$ for the example background state of figure 2 are shown in figure 3b.

258 We can however make analytic progress to find the growth rate in the limit of large
 259 κ (short wavelengths), which is also the relevant limit for examining the short-wavelength
 260 blow-up. Further, figure 3b shows that the large κ limit turns out to provide a good match
 261 to the numerically derived values throughout the range of unstable wavenumbers. We
 262 anticipate that variations in the pressure head will be small, $\hat{h} \ll 1$, so that the $\kappa^2 \hat{h}$
 263 term in (21) remains balanced. We therefore also expect $\sigma - \sigma_0 \ll 1$ as we will be close
 264 to the $\hat{h} = 0$ solution to (19), and so find that $\partial \hat{h} / \partial x \ll \hat{b}$. Finally, in order to keep
 265 all the boundary conditions we must preserve the \hat{b} -derivative in (21), which implies that
 266 $x \ll 1$. Under these assumptions, equation (21) becomes

$$\hat{h} = -\frac{1}{K \kappa^2} \frac{\partial(Q_b \hat{b})}{\partial x}, \quad (22)$$

267 which, substituted into (19), yields

$$\frac{\partial^2(Q_b \hat{b})}{\partial x^2} = \frac{\rho_i K \kappa^2}{M_h} (\sigma - \sigma_0) \hat{b}, \quad (23)$$

268 a single second order differential equation for \hat{b} .

269 With $x \ll 1$, our perturbations are confined to a boundary layer close to the ter-
 270 minus, so we can approximate $Q_b(x)$, $K(x)$, and $M_h(x)$ as constants, and their termi-
 271 nus values. However, since $\sigma - \sigma_0(x)$ is small and changes sign within the boundary layer

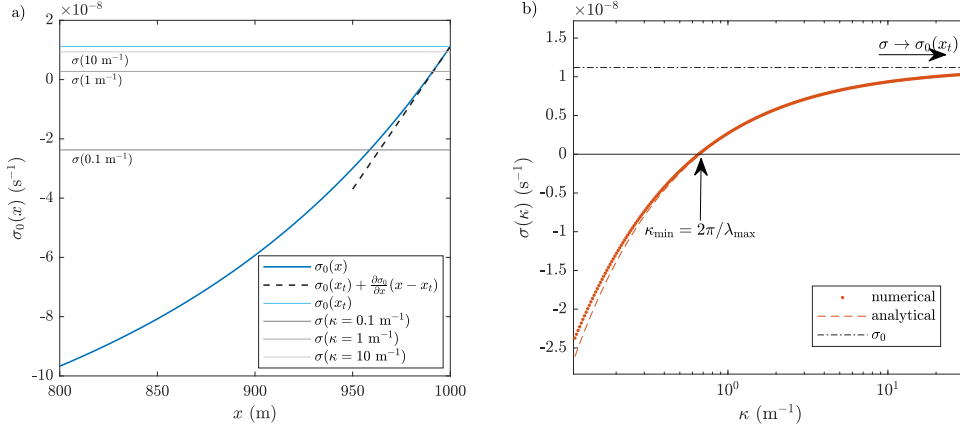


Figure 3. a) The local balance of melt versus collapse, $\sigma_0(x)$, increases towards the terminus and is eventually greater than the growth rate for any given wavenumber. The linearisation close to the terminus is plotted to show the validity of the analytic approach. b) Growth rates of perturbations to the background state shown in figure 2, dots calculated as numerical eigenvalues to (19,21) and dashed line calculated analytically per (28). The agreement between the two curves improves as $\kappa \rightarrow \infty$, the limit for which the analytic result is derived. Wavelengths longer than λ_{\max} (55) are stable, and the shortest wavelengths (largest κ) are the most unstable, tending towards a growth rate of σ_0 per (20).

(figure 3a), we retain the next term in its expansion, which is linear in x . Under these approximations, (23) becomes

$$\frac{\partial^2 \hat{b}}{\partial x^2} = \frac{\rho_i K \kappa^2}{Q_b M_h} \left(\sigma(\kappa) - \sigma_0(x_t) + \frac{\partial \sigma_0}{\partial x} (x_t - x) \right) \hat{b}. \quad (24)$$

Recognising this differential equation structure as Airy's equation, we see that in the limit of small wavelengths, the structure of the gap height perturbation $\hat{b}(x)$ must be a rescaled Airy function. By scaling the growth rate $\sigma - \sigma_0(x_t)$ and the inland distance x using

$$\sigma_0(x_t) - \sigma = S \left(\frac{\partial \sigma_0}{\partial x} \right)^{2/3} \left(\frac{Q_b M_h}{\rho_i K \kappa^2} \right)^{1/3}, \quad x_t - x = \left(\frac{Q_b M_h}{\rho_i K \kappa^2 (\partial \sigma_0 / \partial x)} \right)^{1/3} X, \quad (25)$$

(24) simplifies to

$$\frac{\partial^2 \hat{b}}{\partial X^2} = (X - S) \hat{b}, \quad (26)$$

exactly Airy's equation with a shifted coordinate system, with the rescaled growth rate S setting the shift. Since we require our perturbations decay inland, \hat{b} must be an Airy function of the first kind, i.e. $\hat{b} = Ai(X - S)$, and substituting this into (22),

$$\hat{h} = \left(\frac{Q_b}{K \kappa^2} \right)^{2/3} \left(\frac{\rho_i (\partial \sigma_0 / \partial x)}{M_h} \right)^{1/3} Ai'(X - S). \quad (27)$$

Thus, to match on to atmospheric pressure, S is chosen so that $\hat{h}(0) = Ai'(-S) = 0$, so $S = 1.0187\dots$ and

$$\sigma = \sigma_0(x_t) - 1.0187 \left(\frac{\partial \sigma_0}{\partial x} \right)^{2/3} \left(\frac{Q_b M_h}{\rho_i K \kappa^2} \right)^{1/3}. \quad (28)$$

While there are infinitely many other possible values of z such that $Ai'(-z) = 0$, they are increasingly large, and so associated with smaller growth rates; the associated perturbations are always more stable and less relevant to the dynamics of the system.

Beyond its agreement with the numerically determined eigenvalues, we note two important properties of equation (28), plotted in figure 3b. Firstly, the growth rate increases as $\kappa \rightarrow \infty$, indicating an unphysical breakdown of the governing equations since the shortest wavelengths are the most unstable. Secondly, as $\kappa \rightarrow \infty$, $\sigma \rightarrow \sigma_0(x_t)$ from below, so $\sigma_0(x_t)$ is an upper bound on the growth rate of all scales of perturbations. Thus, the sign of $\sigma_0(x_t)$ determines the overall stability of the system. Substituting the form of M_b from table 1 into expression (20) for σ_0 , we have instability if

$$\frac{2 + \omega|\bar{q}|/\nu}{1 + 2\omega|\bar{q}|/\nu} \rho_w g \bar{q} \left| \frac{d\bar{h}}{dx} \right| > G + u_b \tau_b + \rho_i L \frac{b_r u_b}{l_r} \quad (29)$$

at the terminus. We can interpret the terms on the right hand side as the types of heating that allow the distributed system to persist, while the terms on the left are the heating that occurs primarily in rapid channel flow. Thus, channels develop when the melt-rate enhancement provided by channelised flow is enough to open up areas of significantly higher gap heights, altering the permeability of the subglacial network and feeding back into reduced water pressure and higher collapse rate away from the channels.

With $\omega = 0$, i.e. assuming laminar flow everywhere in the distributed system, equation (29) agrees with the critical discharge condition of I. J. Hewitt (2011).

$$2\rho_w g \bar{q} \left| \frac{d\bar{h}}{dx} \right| > G + u_b \tau_b + \rho_i L \frac{b_r u_b}{l_r}, \quad (30)$$

which came from assuming *a priori* that $\hat{h} = 0$, which we have shown is indeed consistent with the short wavelength limit. Also, since the x scale over which perturbations decay, given by (25), looks like $\kappa^{-2/3}$, and shrinks more slowly than the wavelength in the y direction, $2\pi\kappa^{-1}$, this analysis is consistent with a simpler instability calculation in Schoof (2010) that neglects gradients in x , again highlighting that the behaviour is generic despite slightly different formulations of the system.

A more tractable reframing of (29) comes from using (8) and (9) to rewrite the instability criterion in terms of \bar{N} rather than $d\bar{h}/dx$. Since the criterion is evaluated at the terminus, where $\bar{N} = p_i = \rho_i g H$ is just the ice overburden pressure, while \bar{q} can be estimated from inputs and basal melt over the catchment area, this formulation is easier to evaluate for glaciers. We find instability if

$$\frac{192}{27} \frac{\left(1 + \frac{\omega|\bar{q}|}{2\nu}\right)^4 \left(1 + \frac{2\omega|\bar{q}|}{\nu}\right)}{\left(1 + \frac{\omega|\bar{q}|}{\nu}\right)^2} \rho_w \nu \bar{q}^2 \left[\rho_i L \left(A(\rho_i g H)^n + \frac{u_b}{l_r} \right) \right]^3 > \left(G + u_b \tau_b + \rho_i L \frac{b_r u_b}{l_r} \right)^4, \quad (31)$$

which can be read as a frictional-heat-flux-dependent lower bound on $\bar{q}^2 H^9$ at the terminus, above which channels start to form (figure 4). The instability initiates when either high effective pressures close down the distributed system, or high basal fluxes promote channelised melt, compared to the terms on the right that promote opening of the distributed system. We demonstrate the power of this stability criterion in predicting the behaviour of full numerical simulations of subglacial hydrology in section 4.1. However, the same stability analysis also predicts a numerical breakdown at short wavelengths, which we turn our attention to next.

3 Regularising the short-wavelength dynamics

The unphysical breakdown of models at short wavelengths has been previously noted, and numerically overcome in many ways, from turning off dissipative heating in the distributed system (Werder et al., 2013), imposing a minimum channel width (effectively Sommers et al., 2018), or adding a diffusive term to the gap dynamics (Felden et al., 2023). These approaches seek to minimise the impact of this unphysical behaviour; instead, we

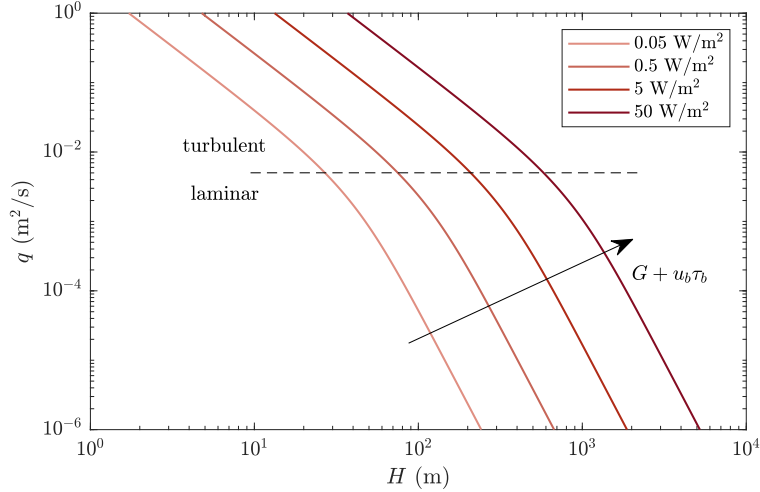


Figure 4. Minimum flux through the terminus (approximately the total volumetric meltwater input, plus melt due to basal heat flux, over the catchment area, divided by the terminus width) needed for channels to initiate, as a function of the ice thickness at the terminus, according to equation (31), for a range of basal heat fluxes $G + u_b \tau_b$. The break-in-slope corresponds to the laminar-turbulent transition in the hydrology model. Opening by sliding is ignored in this plot, but could be included using equation (31).

326 consider the assumptions that introduce the unphysicality in the first place, providing
 327 a more consistent way to regularise the model. We will show, similar to the analysis of
 328 Walder (1982), that by considering in more detail the structure of the thermal profile
 329 in the water layer, a laterally diffusive term appears (this time in the melt-rate) that pro-
 330 vides a physical mechanism for regularisation.

331 To revisit the derivation of the melt-rate in equation (4), we start from the heat
 332 equation

$$\rho_w c_p \left(\frac{\partial T}{\partial t} + \mathbf{u} \cdot \nabla T \right) - k \nabla^2 T = Q, \quad (32)$$

333 where c_p is the specific heat capacity, k is the thermal conductivity and Q is the dissi-
 334 pative heating from the water flow. Since the depth of the water layer is small, we would
 335 expect vertical diffusion of temperature to be the dominant mechanism for heat trans-
 336 port,

$$-k \frac{d^2 T}{dz^2} = Q. \quad (33)$$

337 Depth-integrating this equation, applying the geothermal flux and ice-bed frictional heat-
 338 ing at the base of the water layer, we find that the heat flux into the ice at the top of
 339 the water layer is

$$-k \left. \frac{dT}{dz} \right|_{z=b} = G + |u_b \cdot \tau_b| + \int_0^b Q dz. \quad (34)$$

340 Equating this heat flux with the latent heat flux required to melt the ice, $\dot{m}L$, gets us
 341 back to equation (4) for the melt rate. However, note that the assumption that only the
 342 vertical gradients in temperature are significant breaks down exactly when the wavelengths
 343 become small, and the horizontal scale becomes similar to the vertical. Reintroducing
 344 lateral heat transport is therefore a plausible way to regularise the short-wavelength case.

3.1 Motivation from linearised perturbations

If we introduce perturbations in the vertical temperature profile and dissipative heating, $T = \bar{T}(z) + \hat{T}e^{i\kappa y}$ and $Q = \bar{Q} + \hat{Q}e^{i\kappa y}$, associated with a gap height perturbation $\hat{b}e^{i\kappa y}$, the linearised heat equation (32) becomes

$$\rho_w c_p \left(\frac{\partial \hat{T}}{\partial t} + \bar{u} \frac{\partial \hat{T}}{\partial x} \right) - k \nabla^2 \hat{T} = \hat{Q}. \quad (35)$$

If we consider only long, thin channels and therefore neglect gradients in x , and also neglect the time for the temperature profile in the thin layer to reach equilibrium (relative to timescale of melt), (35) reduces to diffusion of temperature with a heat source,

$$-k \left(\frac{\partial^2 \hat{T}}{\partial z^2} - \kappa^2 \hat{T} \right) = \hat{Q}. \quad (36)$$

The boundary conditions remain a geothermal flux at the base, and that the ice-water interface is at melting temperature, which in terms of the perturbed quantities become

$$-k \left. \frac{\partial \hat{T}}{\partial z} \right|_{z=0} = 0, \quad \left. \frac{\partial \bar{T}}{\partial z} \right|_{z=\bar{b}} \hat{b} + \hat{T}(\bar{b}) = \hat{T}(\bar{b}) - \frac{\bar{m}L}{k} \hat{b} = 0. \quad (37)$$

We solve the linearised diffusion equation (36) with these boundary conditions, and find that the profile of the corresponding temperature change is

$$\hat{T} = \left[\left(\frac{\bar{m}L}{k} \hat{b} - \frac{\hat{Q}}{k\kappa^2} \right) \frac{\cosh(\kappa z)}{\cosh(\kappa \bar{b})} + \frac{\hat{Q}}{k\kappa^2} \right] e^{i\kappa y + \sigma t}, \quad (38)$$

and in particular the additional heat flux into the ice is

$$-k \left. \frac{\partial \hat{T}}{\partial z} \right|_{z=\bar{b}} - k \left. \frac{\partial^2 \bar{T}}{\partial z^2} \right|_{z=\bar{b}} \hat{b} = \frac{\tanh(\kappa \bar{b})}{\kappa} \hat{Q} + (\bar{Q} - \kappa \tanh(\kappa \bar{b}) \bar{m}L) \hat{b}, \quad (39)$$

which, equating to the latent heat of melting $\hat{m}L$, corresponds to a melt-rate perturbation

$$\hat{m} = \frac{1}{L} \left(\frac{\tanh(\kappa \bar{b})}{\kappa} \hat{Q} + (\bar{Q} - \kappa \tanh(\kappa \bar{b}) \bar{m}L) \hat{b} \right). \quad (40)$$

To simplify this further, we consider the case where the background gap height is small, so $\tanh(\kappa \bar{b}) \approx \kappa \bar{b}$. Then (40) becomes

$$\hat{m} = \frac{1}{L} \left(\hat{Q} \bar{b} + \bar{Q} \hat{b} \right) - \kappa^2 \bar{b} \bar{m} \hat{b} = \hat{m}_0 - \kappa^2 \bar{b} \bar{m} \hat{b}, \quad (41)$$

where \hat{m}_0 is the perturbation in melt-rate when ignoring lateral heat transport, previously found in equation (18). We see that including lateral diffusion of heat has introduced a new term proportional to $-\kappa^2 \hat{b}$, which has the structure of a diffusion of gap height away from narrowly channelising regions, sufficient to regularise the linear stability analysis. Equation (41) is structurally similar to equation (14) of Walder (1982), although the rest of that analysis proceeded to neglect the diffusion term, arguing it was too small to impact the water layer dynamics.

Equation (41) is enough to continue with the regularised linear stability and to demonstrate that temperature diffusion is key to resolving the width of channels. However, for the purposes of numerical simulation beyond the initial onset of channels, we seek a non-linear representation of the impact of lateral heat transport, a simplification of (32) that retains these dynamics without resolving the full 3-dimensional temperature structure in the water layer. From the structure of the new term, $-\kappa^2 \bar{b} \bar{m} \hat{b}$, it would appear that the melt-rate expression (4) is missing a term similar to $\nabla \cdot (\hat{m} b \nabla b)$, which we seek in the next section.

376

3.2 Deriving a non-linear diffusion term

377

378

379

380

To find the melt-rate at the ice-water interface, we need the heat flux into the ice, which comes from an integral of the heat fluxes in the water layer. However, rather than integrating the simpler (33), which ignores lateral temperature diffusion, we integrate the full steady heat equation (32) and obtain

$$-bk\nabla_H^2\bar{T} = G + k\left.\frac{\partial T}{\partial z}\right|_{z=b} + |u_b \cdot \tau_b| + \int_0^b Q dz. \quad (42)$$

381

382

where \bar{T} denotes the depth-averaged temperature of the water and ∇_H denotes horizontal gradients.

383

384

385

386

387

388

Since we are now considering how the melting of sloping interfaces can act to widen channels, we draw a distinction between \dot{m} , the rate at which the interface appears to move upwards (appearing in the expression for the motion of the interface, equation (2)), and \dot{M} , the rate at which the interface moves in the direction normal to itself due to melting. These two rates are geometrically linked via the slope of the interface, $\dot{m} = \sqrt{1 + (\nabla_H b)^2} \dot{M}$. Physically, the heat flux into the interface balances the melting into the interface, so

$$\dot{M}L = -\frac{k}{\sqrt{1 + (\nabla_H b)^2}} \left(\frac{\partial T}{\partial z} - \nabla_H b \cdot \nabla_H T \right). \quad (43)$$

389

390

Rearranging (43) to obtain the vertical temperature gradient in terms of \dot{m} and the horizontal temperature gradients, and inserting this into (42), we obtain

$$\dot{m}L - \nabla_H \cdot (bk\nabla_H T) = G + |u_b \cdot \tau_b| + \int_0^b Q dz. \quad (44)$$

391

392

393

The new terms represent the lateral transport of heat via diffusion, so that melt-rate is not only dependent on the local dissipation rate, but also on the heating in neighbouring areas.

394

395

396

397

Since all the ice is assumed to be at the melting temperature, $T(b) = T_m$. Thus if there are horizontal variations in T close to the ice interface, they can be directly related to changes in the distance to that interface, and so by applying the chain rule for differentiation we find

$$\nabla_H T = -\frac{\partial T}{\partial z} \nabla_H b. \quad (45)$$

398

399

400

401

We can use this to write the melt-rate in (43) purely in terms of vertical temperature gradients, and thus re-express the horizontal temperature diffusion in (44) as a melt-rate diffusion instead, avoiding the need to resolve the temperature field in simulations. After some rearranging, and inserting the form of the dissipative heat flux, we arrive at

$$\dot{m} = \frac{1}{L} (G + |u_b \cdot \tau_b| - \rho_w g \mathbf{q} \cdot \nabla h) + \nabla_H \cdot \left(\frac{b\dot{m}\nabla_H b}{1 + |\nabla_H b|^2} \right). \quad (46)$$

402

403

404

405

406

This is the same as our original melt-rate equation (4), but with a new, non-local, melt-diffusion term that allows areas of high local heat fluxes to also cause melting in their surroundings. We still only need to simulate the gap height, pressure head, and melt-rate, so (46) can be used with equations (1-3) to simulate subglacial hydrology exactly as before.

407

408

409

410

411

412

The non-linear version of the melt-diffusion term in (46) reassuringly agrees with the form anticipated from the linearised analysis (41). The term is also somewhat similar in structure to the gap-height diffusion term introduced in Felden et al. (2023), with two key differences. Firstly, the full melt-rate is included in the diffusivity here, rather than only the dissipative contributions. This distinction is less important in regions with high basal water flux, but more significant where geothermal flux dominates. Secondly,

413 as a structural difference, it appears directly in the expression for the melt-rate, and is
 414 not just used to regularise one of the evolution equations for b . However, the precedent
 415 set by Felden et al. (2023) gives confidence that a diffusional term of this nature is suf-
 416 ficient to dampen the short-wavelength blow-up, as we show in the next section.

417 3.3 Regularised linear stability analysis

418 We now resume with the linear stability analysis including the melt-rate diffusion
 419 term derived in (41), which we have just shown is also the linearisation of the full mod-
 420 ified melt-rate equation. We expect much of the previous analysis to carry through ex-
 421 actly, but that the growth rate at the shortest wavelengths will be reduced.

422 With the new melt-diffusion term modifying the melt-rate perturbation from (18)
 423 into (41), the equations (19) and (21) for the structure of the pressure head \hat{h} and gap
 424 height \hat{b} perturbations are slightly modified to

$$\left(\sigma - \frac{M_b}{\rho_i} + A\bar{N}^n + \frac{u_b}{l_r} + \frac{\bar{m}\bar{b}}{\rho_i}\kappa^2\right)\hat{b} = \left(An\bar{N}^{n-1}\rho_w g\bar{b} - \frac{U}{\rho_i}\right)\hat{h} - \frac{M_h}{\rho_i}\frac{\partial\hat{h}}{\partial x} + \frac{\partial}{\partial x}\left(\frac{\bar{m}\bar{b}}{\rho_i}\frac{\partial\hat{b}}{\partial x}\right), \quad (47)$$

425 and

$$\sigma\hat{b} = -\frac{\partial}{\partial x}\left(Q_b\hat{b} - Q_h\frac{\partial\hat{h}}{\partial x}\right) - K\kappa^2\hat{h} + \frac{M_b}{\rho_w}\hat{b} - \frac{U}{\rho_w}\hat{h} - \frac{M_h}{\rho_w}\frac{\partial\hat{h}}{\partial x} - \frac{\bar{m}\bar{b}}{\rho_w}\kappa^2\hat{b} + \frac{\partial}{\partial x}\left(\frac{\bar{m}\bar{b}}{\rho_w}\frac{\partial\hat{b}}{\partial x}\right). \quad (48)$$

426 This is once again an eigenvalue problem to find the growth rate σ corresponding to \hat{h}
 427 and \hat{b} which can only be solved numerically in general (figure 5).

428 However, if we anticipate only a small change from our previous analysis, we can
 429 go through the same simplifications and once again look primarily at the large κ (small
 430 wavelength) case, taking the same limit of small pressure variations, $\hat{h} \ll 1$, and chan-
 431 nels confined close to the terminus, $1/\kappa \ll x \ll 1$. Under these assumptions, equa-
 432 tions (47-48) reduce to

$$\left(\sigma - \frac{M_b}{\rho_i} + A\bar{N}^n + \frac{u_b}{l_r} + \frac{\bar{m}\bar{b}}{\rho_i}\kappa^2\right)\hat{b} = -\frac{M_h}{\rho_i}\frac{\partial\hat{h}}{\partial x}, \quad (49)$$

433 and

$$K\kappa^2\hat{h} = -Q_b\frac{\partial\hat{b}}{\partial x}. \quad (50)$$

434 These are structurally identical to the previous large κ limit, but with an additional $\bar{m}\bar{b}\kappa^2/\rho_i$
 435 multiplying \hat{b} in (49). This means σ_D , the growth rate when $\hat{h} = 0$, is now

$$\sigma_D = \frac{M_b}{\rho_i} - A\bar{N}^n - \frac{u_b}{l_r} - \frac{\bar{m}\bar{b}}{\rho_i}\kappa^2 = \sigma_0(x_t) - \frac{\bar{m}\bar{b}}{\rho_i}\kappa^2 \quad (51)$$

436 and becomes stable as κ gets large. This modifies the overall growth rate found in (28)
 437 to

$$\sigma = \sigma_0(x_t) - \frac{\bar{m}\bar{b}}{\rho_i}\kappa^2 - 1.0187\left(\frac{\partial\sigma_0}{\partial x}\right)^{2/3}\left(\frac{Q_bM_h}{\rho_iK\kappa^2}\right)^{1/3}, \quad (52)$$

438 which, as shown in figure 5, is stable at both the largest and smallest wavenumbers.

439 Importantly, we now have a maximum growth rate at a finite value of κ , since σ
 440 decreases quadratically as κ gets large, we have regularised the short wavelength singu-
 441 larity. The most unstable wavenumber is at approximately

$$\kappa = \left(\frac{1.0187\rho_i}{3\bar{m}\bar{b}}\right)^{3/8}\left(\frac{\partial\sigma_0}{\partial x}\right)^{1/4}\left(\frac{Q_bM_h}{\rho_iK}\right)^{1/8}. \quad (53)$$

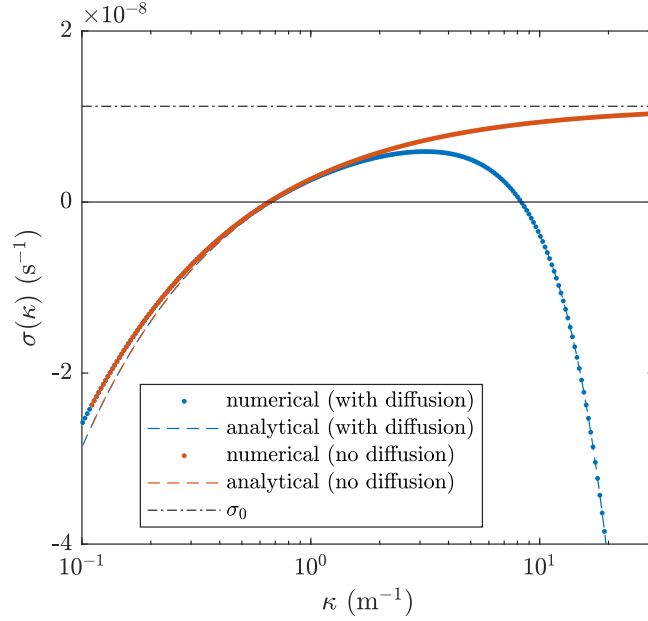


Figure 5. Impact of including diffusion on the growth rates of perturbations. In red, the original model, as in figure 3b. In blue, the modified growth rates including melt-diffusion: dots are numerical eigenvalues of (47,48) and dashed line shows the analytic growth rate (52). The shortest wavelengths are now stabilised and there is now a peak in the growth rate at (54) an intermediate wavenumber given by (53).

442 While this wavelength is small (comparable to the thickness of the water layer), there
 443 is no longer an unphysical breakdown in the predicted behaviour. The maximum growth
 444 rate is slightly reduced by the diffusive effects to

$$\sigma = \sigma_0(x_t) - 4 \left(\frac{\bar{m}\bar{b}}{\rho_i} \right)^{1/4} \left(\frac{1.0187}{3} \right)^{3/4} \left(\frac{\partial\sigma_0}{\partial x} \right)^{1/2} \left(\frac{Q_b M_h}{\rho_i K} \right)^{1/4}, \quad (54)$$

445 as can be seen in figure 5, the maximum growth rate is somewhat less than σ_0 . However,
 446 the stability criterion (31) based only on $\sigma_0(x_t)$ still holds to good approximation (e.g.
 447 figure 6a).

448 With our improved set of governing equations, we see that they now produce wave-
 449 length selection. We next perform numerical simulations of the equations to demonstrate
 450 both the validity of our analysis and to illustrate the power of linear stability analysis
 451 for predicting the behaviour of subglacial hydrology without resorting to full numerical
 452 simulation.

453 4 Simulations results and discussion

454 We implemented the SHAKTI governing equations, with the additional melt-diffusion
 455 term, in the adaptive-mesh PDE solver Basilisk (Popinet, 2013–2024) using the inbuilt
 456 Poisson solver to calculate the pressure head and flux, and an explicit fixed time-step
 457 forward Euler method to update the gap height. The subglacial geometry and melt-rate
 458 are only updated during the explicit time-step, and kept at this value during the follow-
 459 ing Poisson solve routine. The mesh adaptation and interpolation are handled by the
 460 adapt routine of Basilisk. The adaptive mesh allowed us to locally reach much higher
 461 resolutions than possible in the original ISSM implementation of SHAKTI (Sommers et

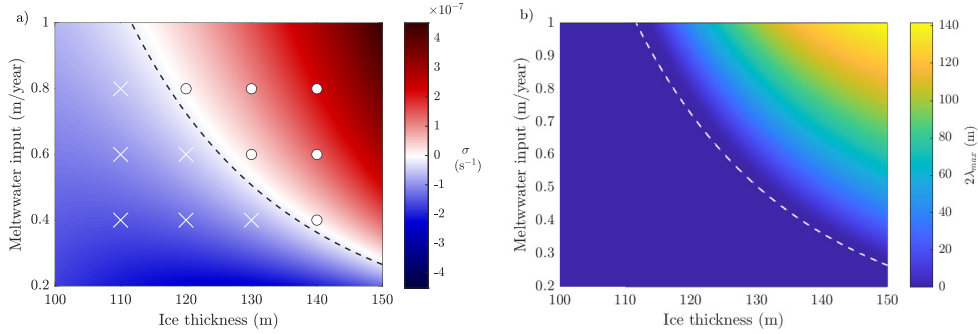


Figure 6. a) effect of varying meltwater input and ice thickness on three metrics of channelization. Dashed line gives the approximate stability criterion (31), where we use total meltwater input and geothermal melting only to estimate of flux at the terminus. Color shows maximum growth rate predicted by (54), using a 1D calculation of \bar{q} that includes dissipative melt at the bed. Outcomes from the full numerical simulations are superimposed - crosses indicate no channels, circles indicate channels developed. When the maximum predicted growth rate is positive, channelization is indeed observed. The boundary predicted by (31) lies just inside the stable regime according to (54) due to the impact of melt-diffusion, which is not considered in (31). b) predicted minimum mesh side length needed to resolve instability, equal to $2\lambda_{\max}$, from (55). Regions without instability are shown as 0. Channels are most vulnerable to numerical suppression close to the margin of stability, when the required mesh size gets small.

462 al., 2018), and without having to specify possible channel locations beforehand as in GlaDS
 463 (Werder et al., 2013).

464 We perform the majority of our simulations in the same idealised test geometry as
 465 Sommers et al. (2018), a 1km square domain with uniform ice thickness and slope of 0.02
 466 towards the outflow boundary, at which we impose atmospheric pressure, while the other
 467 three sides of the domain are no-flux boundaries. We focus on a test case that is close
 468 to the stability boundary, 120m-thick ice with distributed meltwater input of 0.8m per
 469 year throughout the domain (matching the scenario presented in figures 2, 3 and 5 of this
 470 paper). The simulations are initiated with a gap height in the range 0.9-1 mm, independ-
 471 ently selected from a uniform random distribution for each mesh cell. The simulations
 472 rapidly converge to something close to the laterally-uniform base state, with small devi-
 473 ations away from this localised near the terminus.

474 4.1 Channel initiation is a predictable linear process

475 Varying the surface meltwater input and ice thickness, the growth rate (52) suc-
 476 cessfully predicts whether or not channels develop in numerical simulations (figure 6a),
 477 and the simpler stability criterion (31) also performs well. Channelization occurs if the
 478 flow-rate within the channels is high, especially if strong creep-closure elsewhere prevents
 479 water from leaving through the distributed system. Thus, we see channels form when
 480 the rate of meltwater input is large (high dissipative heating and local melt keeps the
 481 channels open) and when the ice sheet is thicker (ice overburden pressure promotes clo-
 482 sure and tamps down on the distributed system). The stability criterion (31) depends
 483 only on the glacier geometry and estimates of net surface meltwater input within the catch-
 484 ment area. As it can be quickly evaluated, it provides a quick estimate of the charac-
 485 ter of subglacial flow to compare with spatio-temporal patterns of glacier velocity, with-
 486 out running a full numerical simulation.

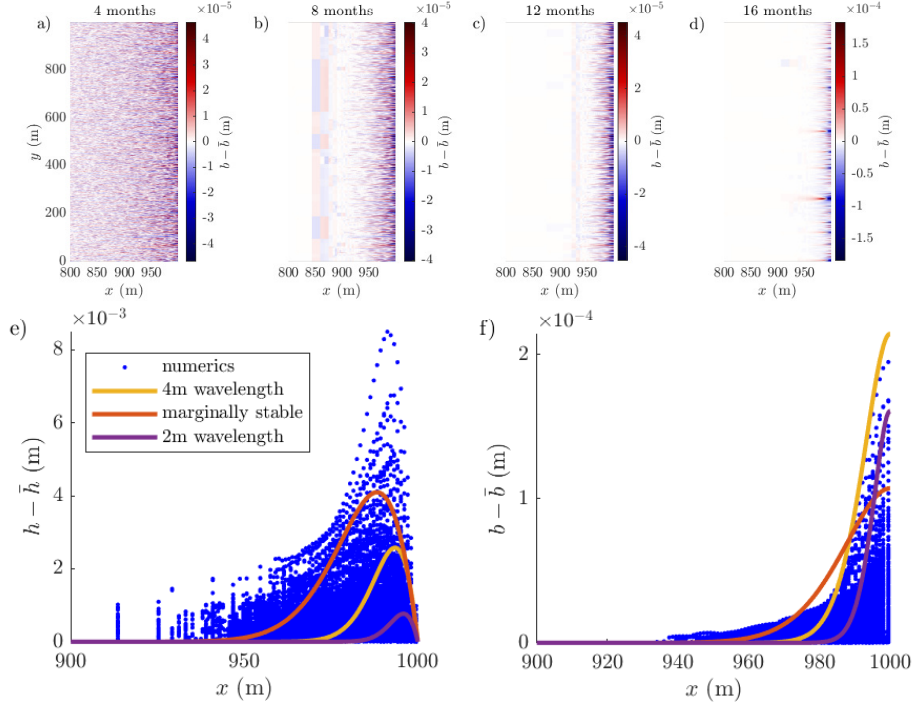


Figure 7. a-d), evolution of the deviation in gap height away from the width-averaged value. Initially, the deviation is due to the random noise introduced everywhere in the domain. The perturbations with the largest lengthscales are stable and thus decay away, leaving only the narrow fluctuations close to the terminus. These small-scale perturbations are unstable and grow into channels propagating back into the interior of the domain. The larger scale blocks seen ~ 200 m from the terminus are artefacts from mesh adaptation. e-f), comparison between the numerical deviation from average pressure head (e) and gap height (f) at 12 months, and the Airy eigenfunctions for a range of unstable wavelengths. The relative size of \hat{h} and \hat{b} is set by (27), and thus the agreement in both amplitude and shape give additional confidence in the analytic results. The persistence into the interior and the somewhat larger $h - \bar{h}$ than predicted can be attributed to longer wavelength, stable modes that are still decaying away.

Beyond the stability criterion, the structure of the variations in gap height and water pressure are also well-predicted by the stability analysis. In the unstable cases, the initial perturbations first develop close to the margin of the ice sheet, at a wavelength comparable to the most unstable mode (53). The along-flow structure of the growing gap-height and water-pressure perturbations match the shapes predicted by the Airy eigenfunctions (figure 7), with large variability close to the margins, decaying inland. This suggests that channels are more likely close to termini (in agreement with observations and simulations; Werder et al., 2013; Poinar et al., 2019) as they initiate in this near-terminus region of large pressure perturbations and then propagate inland.

4.2 Channel configuration cannot be predicted from linear theory

As the perturbations develop and propagate inland, they become non-linear features: large, distinct channels surrounded by almost fully-drained areas of distributed flow, far from a small perturbation in sheet depth. These features evolve according to the equations for R othlisberger channels (see Appendix A). The interactions between neighbouring channels involve complex, long-range competition for the meltwater being delivered from the surface, and rapid growth expanding into space vacated by the channels that lose out in this competition and suddenly collapse (video in supplementary). As such, the dynamics that govern the evolution of channel spacing cannot be explained using linear stability analysis. The most unstable wavelength, despite its importance to the early-time patterns of channels, is not visible in the final configuration of the subglacial hydrology.

Predicting the number of channels in a catchment area, their average spacing, and net effect on the subglacial water pressure remains challenging. From an analysis of the pressure distribution around a single, non-evolving channel, I. J. Hewitt (2011) suggested that the spacing of channels should be similar to their length. Our final configurations show a somewhat smaller spacing (e.g. in figure 8, around one third of their length). Overall, being able to predict the evolution of average properties of the subglacial system (such as channel spacing and effective pressure) without simulating individual channels is a goal for reduced modeling. Numerical simulations can provide an important inspiration for the development of such models, but are vulnerable to producing numerical artefacts, an example of which we discuss below.

4.3 Minimum resolution requirement

For coupled ice-hydrology models, we would ideally simulate the subglacial hydrology at the same resolution as that of ice flow, i.e. on a grid at the kilometre scale. However, the resolution of numerical simulations can dramatically impact the behavior of the simulated water flow. Since long wavelengths are always stable (figures 3b and 5) due to the scale of pressure gradients they induce, simulations on a coarse grid may appear stable even in a regime where instability is expected. The maximum unstable wavelength,

$$\lambda_{\max} = 6.11 \left(\frac{\rho_i K}{Q_b M_h} \right)^{1/2} \frac{\sigma_0(x_t)^{3/2}}{\partial \sigma_0 / \partial x}, \quad (55)$$

found by setting the growth rate in (28) to 0, controls the scale above which any disturbances decay away. If the smallest scales resolved by the simulation are larger than this wavelength, the numerical simulation will not produce instability, since the only drivers of channelization would occur on smaller scales than can be resolved. Thus, we find channels can be suppressed numerically in situations where a physical balance would predict instability. This results in the persistence of an inefficient drainage system, leading to an overestimate of basal water pressure (figure 8).

To illustrate this effect, we simulated the same idealised test case across a range of maximum grid resolutions. We deliberately chose a configuration that was only just

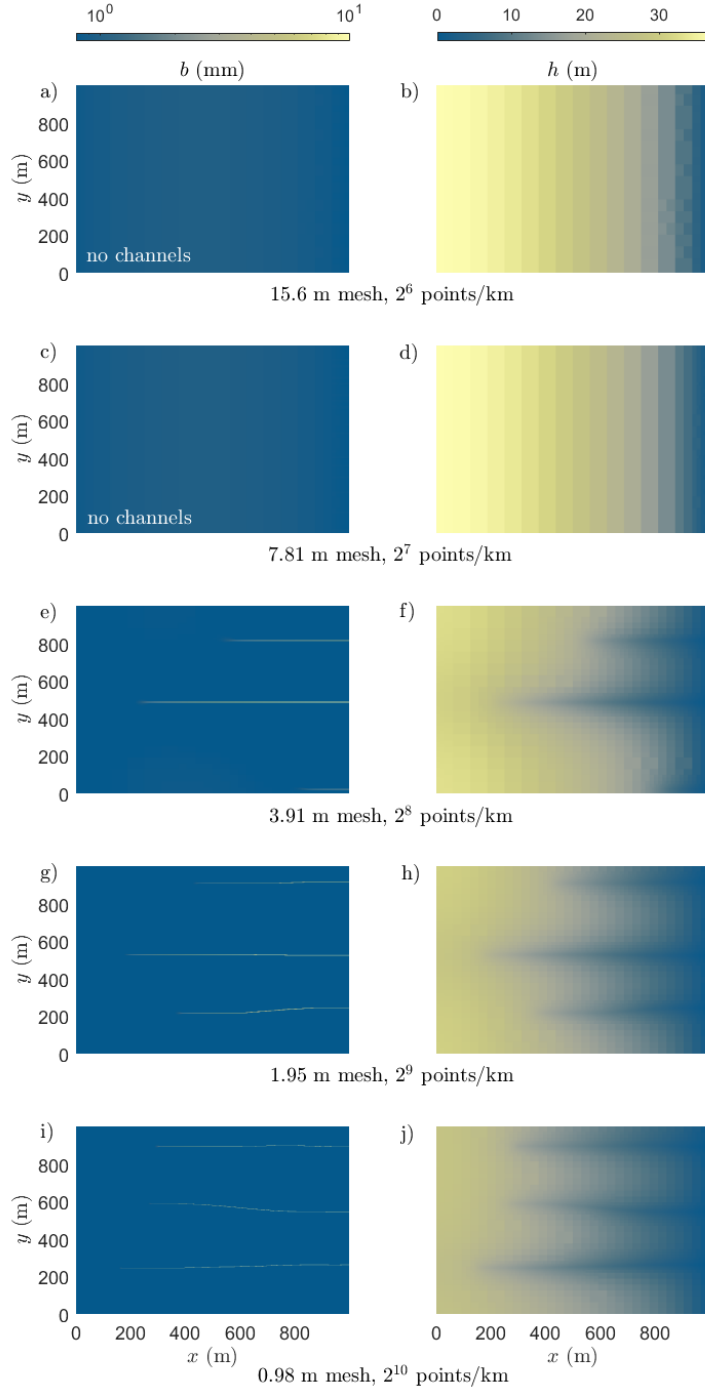


Figure 8. The impact of varying resolution on the state of the simulated subglacial hydrology after 10 years of simulation time. Minimum mesh size halves with each plot from top to bottom. Left panels show gap height b (in mm, log colorscale), and right the corresponding pressure head h (in m). The channels are regions of lower water pressure compared to the surrounding regions, pulling meltwater from their surroundings and funnelling it towards the margin (right hand side of domain). Large meshes suppress channelization and result in higher inland water pressures. The final channel spacing, unrelated to the linear initiation, emerges as neighbouring channels compete and migrate inland (video in supplementary).

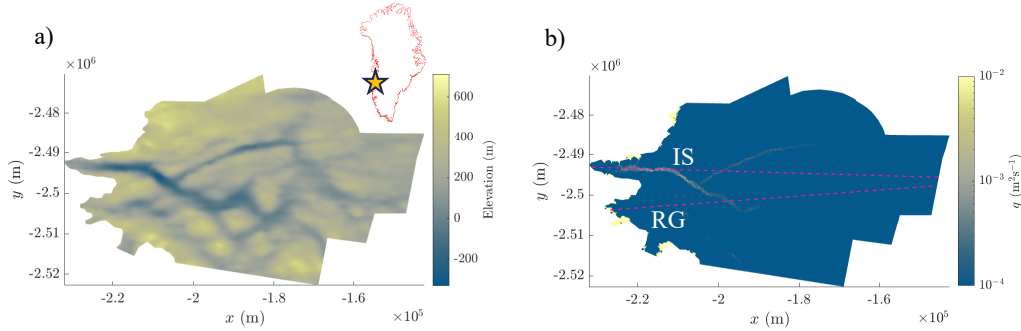


Figure 9. a) Topography beneath Russell Glacier (RG) and Isunnguata Sermia (IS). The inset shows the location in southwest Greenland. b) Subglacial water flux beneath RG and IS under winter conditions, as simulated in SHAKTI. A channel develops beneath IS following the lows in basal topography (Morlighem et al., 2017). Dashed lines indicate the profiles of topography and ice thickness used for the stability calculations.

534 unstable, leading to a fairly small value of $\lambda_{\max} = 9.52$ m according to (55). Basilisk
 535 requires the number of gridpoints to be a power of 2, so for our 1km domain we tested
 536 meshes from $1000/2^6 = 15.625$ m to $1000/2^{10} = 0.977$ m. Channelization was sup-
 537 pressed by the 15.6m and 7.81m meshes, but occurs with the 3.91m mesh and smaller,
 538 since at this mesh size and below at least two grid points fit within an unstable wave-
 539 length and an unstable oscillation can be simulated (figure 8).

540 Although simulating a full glacier at a resolution below 4m is currently unreason-
 541 able, figure 6b shows that the minimum resolution required to capture the instability grows
 542 rapidly, to a scale of hundreds of metres, as we move away from the stability boundary.
 543 Thus, caution is only needed close to the onset of channel formation. Even a relatively
 544 low-resolution model will predict channelization if the system is unstable enough.

545 However, figure 8 also demonstrates that even when channel formation is captured,
 546 the inland extent and spacing of the channels remain grid-dependent until the width of
 547 the channels is well-resolved. Without melt-diffusion, channels remain one grid-cell wide
 548 (c.f. Felden et al., 2023) and the channel spacing never converges. Including the melt-
 549 diffusion term allows for finite width channels and for the channel distribution to con-
 550 verge, but requires resolutions higher than the width of channels (c.f. Appendix B1).

551 4.4 Relevance to more realistic scenarios

552 The configuration we study here is idealised in two main ways: the simple, laterally-
 553 uniform geometry, and the meltwater input that is kept constant in time. In the sim-
 554 ulations shown in figure 8, the meltwater input is kept constant over a timescale of years
 555 to allow the channels to fully develop to a steady configuration, a poor representation
 556 of seasonal melt for Greenland and mountain glaciers. In part, this is due to our focus
 557 on conditions close to marginal stability, where the growth rates of instabilities are small.
 558 In more unstable configurations, the growth rate (figure 6) is orders of magnitude larger,
 559 so channels develop on a timescale of weeks. This illustrates that it is not only the sign
 560 of the maximum growth rate (54), but also its magnitude, that controls whether large
 561 channels develop during a melt season. To explain the the seasonal patterns of subglacial
 562 hydrology, we would need to look at the total time-integrated growth rate with varying
 563 meltwater input, to assess if and when the first channel-sized features appear. We leave
 564 this for future work.

Our simplified geometry allows us to perform stability analysis using a background state that is uniform across the width of the terminus, leading to the appearance of self-selecting, randomly distributed perturbations across the domain. The basal topography of real glaciers and ice streams is heterogeneous at a range of scales, guiding both the location of channel initiation and the pathways in the final channel configuration. However, our analysis still highlights the fundamental competition between channelising melt and viscous ice collapse that governs the question of channelization. Thus, we may still be able to predict which glaciers are likely to feature an efficient subglacial network based on a representative assessment of criterion (31) at the glacier terminus.

As a demonstration, we ran SHAKTI in the ISSM framework on a domain including Russell Glacier (RG) and Isunnguata Sermia (IS) in Southwest Greenland under winter (no meltwater input) conditions (per Sommers et al., 2023), using geometry from Bed-Machine v4 (Morlighem et al., 2017) and velocities from MEaSURES (Joughin et al., 2018). As shown in figure 9, a channel forms under IS but not under RG. We compare this to the maximum growth rate of instabilities based on 1D profiles down the midlines of each glacier (dashed lines on figure 9). We find a positive growth rate of $1.33 \times 10^{-7} \text{s}^{-1}$ at IS, consistent with channel development. At RG, which has thinner ice at the terminus, the maximum growth rate is $-6.79 \times 10^{-8} \text{s}^{-1}$. The negative value indicates that distributed flow is indeed expected during the winter. These results indicate that linear stability analysis can provide a characterisation of subglacial hydrology even in more complex domains.

5 Conclusions

To better understand both the channelization of subglacial hydrology and numerical models thereof, we have performed a full linear stability analysis of distributed subglacial flow, finding a stability criterion and the growth rates of different scales of perturbations.

We confirmed the existence of a short-wavelength blow-up in the original model of distributed water flow, under which channels would always narrow unphysically to the smallest scale of the simulation. We have demonstrated that consistent, convergent simulated behaviour can be achieved through the re-introduction of lateral temperature diffusion to the model, and have derived a melt-rate diffusion term to parameterise this effect, allowing for its smooth integration into existing modeling frameworks. We also showed that long wavelength perturbations are always stabilised, due to the large pressure gradients they induce, and thus derived a minimum resolution requirement (55) below which numerical models are unable to resolve the onset of channelization.

Importantly, we have demonstrated that channels initiate when the enhanced melt due to heat produced by flow inside a channel overwhelms the balance between geothermal and viscous ice collapse that controls the distributed flow network. This criterion (31) provides a rapid estimate of when an efficient subglacial system is expected to form, and thus opens a path for understanding the seasonal trends of glacier velocity and their possible changes in a warming climate, without recourse to a full numerical model.

Appendix A Recovery of R othlisberger channel behaviour

When adding lateral heat diffusion to the SHAKTI equations, the width of the channels is no longer grid-size dependent but converges to a finite width (figure B1). The channels that develop are approximately semi-circular in cross-section, and their width scales like their maximum height. In this section we show that the evolution of these self-selecting features is comparable to the behaviour of R othlisberger channels in models for which separate equations are imposed for the distributed and channelised portions of the domain.

614 Integrating mass conservation (1) across a channel of width w , we get

$$\frac{\partial S}{\partial t} + \frac{\partial Q_c}{\partial x} = -\frac{\partial q_y}{\partial y} + \frac{\dot{M}_c}{\rho_w} + i_{eb}w, \quad (\text{A1})$$

615 where S is the cross-sectional area of the channel, Q_c is the total flux through the chan-
 616 nel, \dot{M}_c is the total melt on the channel wall, $\Omega = -\partial q_y / \partial y$ is the input of meltwater
 617 from the distributed system, and $i_{eb}w$ is the input of surface meltwater landing directly
 618 in the channel, which we can neglect, to get

$$\frac{\partial S}{\partial t} + \frac{\partial Q_c}{\partial x} = \Omega + \frac{\dot{M}_c}{\rho_w}, \quad (\text{A2})$$

619 along with the integral of (2) which gives

$$\frac{\partial S}{\partial t} = \frac{\dot{M}_c}{\rho_i} - AN^n S. \quad (\text{A3})$$

620 Integrating the melt equation, we have

$$\dot{M}_c = \frac{1}{L} \left((G + |u_b \cdot \tau_b|)w - \rho_w g Q_c \frac{\partial h}{\partial x} \right) \quad (\text{A4})$$

621 but if we again neglect the background terms (proportional to w) as small compared to
 622 the dissipative melting, we arrive at

$$\dot{M}_c = \frac{Q_c}{L} \frac{\partial h}{\partial x} \quad (\text{A5})$$

623 To find the flow law giving Q_c , we rely on the observation that diffusion guaran-
 624 tees that the width of a channel scales like its height, since for a long, quasi-steady chan-
 625 nel

$$0 = \frac{\dot{m}}{\rho_i} - AN^n b + \frac{\partial}{\partial y} \left(\frac{\dot{m} b}{\rho_i} \frac{\partial b}{\partial y} \right), \quad (\text{A6})$$

626 and therefore if melt is large, $b \sim y$. Thus, integrating (3) in the limit of high Re , we
 627 have

$$Q_c = \frac{S(g|\nabla h|)^{1/2}}{(12f\omega)^{1/2}} \quad (\text{A7})$$

628 where f is a shape factor relating the integral of depth-cubed across the width of the chan-
 629 nel to S^2 , since both scale like b^4 , but the shape factor will depend on the exact shape
 630 of the channel (for semi-circular channels, $f = 2\pi/3$).

631 Equations (A2, A3, A5) are exactly the conservation equations expected for R othlisberger
 632 channels, while (A7) is similar up to the choice of power on S . Here we arrive at $\alpha_c =$
 633 1, while (Werder et al., 2013) use $\alpha_c = 5/4$. If we took b^4 in (3), we could arrive at the
 634 same α_c .

635 **Appendix B Validation of Basilisk implementation**

636 **B1 Comparison to SUHMO: single convergent channel**

637 We implemented the same channelising test case as in SUHMO (Felden et al., 2023),
 638 a 64 m domain with a bedslope of 0.02 and a slab of ice of constant 500 m thickness. A
 639 moulin delivering $30\text{m}^3\text{s}^{-1}$ of water is located 16 m from the margin with a Gaussian
 640 profile in space. The moulin input is gradually increased in time, from 0 at time $t = 0\text{s}$
 641 to the maximum value after about a month, and the simulation proceeds until steady
 642 state is reached.

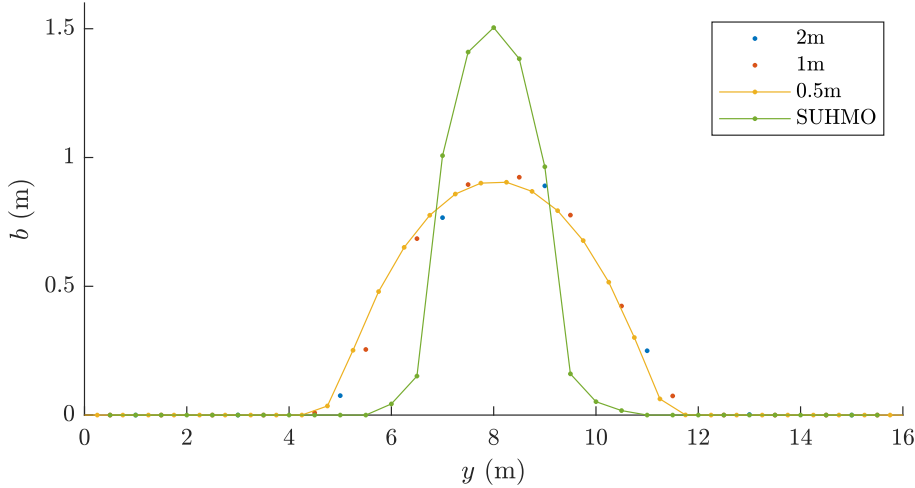


Figure B1. Gap height b at a transect 10m inland of the margin, when a large moulin is located 16m inland of the margin. We see convergence in channel width and height with increasing resolution. The same example in SUHMO produces a taller, narrower channel, as expected. Without any melt-diffusion, the channel would be one grid cell wide.

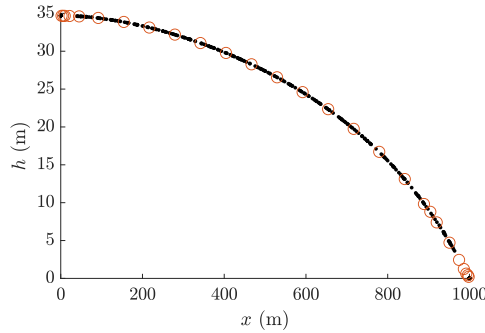


Figure B2. Pressure head from the ISSM (black dots) and Basilisk (red circles) implementations of SHAKTI show complete agreement throughout the domain in the distributed case (with 0.6m/year of meltwater input, 120 m thick ice, after 10 years of simulation time.)

643 Similarly to the SUHMO results, the channel converges towards a fixed height and
 644 width with increasing numerical resolution (figure B1). We produce a wider, less tall chan-
 645 nel than in SUHMO (6 m vs 3 m wide, 0.9m vs 1.5m high) due to the higher diffusiv-
 646 ity that includes the geothermal flux, promoting enhanced widening rates in the chan-
 647 nels.

648 B2 Comparison to ISSM

649 We simulated the 120m ice, 0.6m/year melt configuration in both the ISSM and
 650 Basilisk implementations of SHAKTI. This case is predicted not to channelise (figure 6),
 651 providing a test of the Poisson solver, as both should converge towards the same later-
 652 ally uniform state. Indeed, we found the same distributions of pressure head and gap height
 653 in both implementations (figure B2).

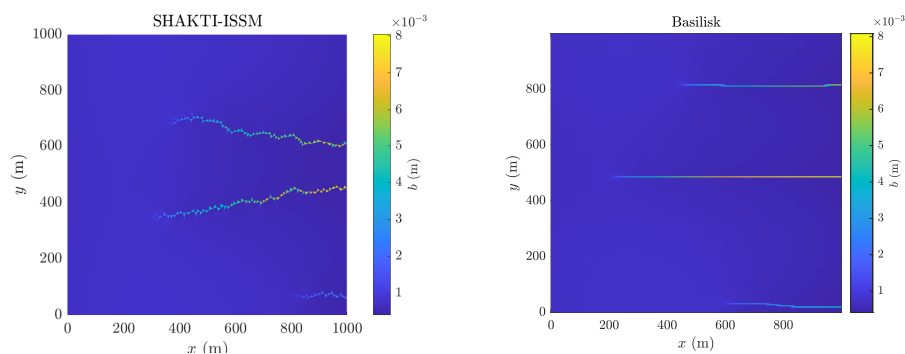


Figure B3. Channels that developed in a 1km square domain, with 0.8m/year of meltwater input, 130 m thick ice, after 10 years of simulation time. a) With the ISSM implementation of SHAKTI, using an average mesh side length of 5 m, b) with the Basilisk implementation of SHAKTI, and a minimum mesh size of 3.91 m.

654 We then tested 130m thick ice with 0.8m/year of meltwater, which as predicted results in channels in both the ISSM and Basilisk implementations (figure B3). Both simulations developed two large channels and one small channel. The location of the channels differs between simulations, which is to be expected from the randomly seeded initial perturbation.

659 These two experiments give confidence that our Basilisk implementation of the SHAKTI governing equations is correct.

661 Open Research Section

662 Code for calculating the laterally uniform profiles, eigenfunctions, and growth rates, is available at <https://zenodo.org/doi/10.5281/zenodo.10887090>. Basilisk is available at <http://basilisk.fr/src/INSTALL> and the Basilisk implementation of SHAKTI is available at <https://zenodo.org/doi/10.5281/zenodo.10887093>. ISSM, including an implementation of SHAKTI, is available at <https://issm.jpl.nasa.gov/>. MEaSUREs velocity data is available at <https://nsidc.org/data/nsidc-0670/versions/1>. BedMachine is available at <https://nsidc.org/data/idbmg4/versions/4>.

669 Acknowledgments

670 KLPW was funded by the Dartmouth Society of Fellows; CRM acknowledges funding from NSF (2012958), NASA (EPSCoR-80NSSC21M0329), the Army Research Office (78811EG), and the Heising-Simons Foundation (2020–1911); and ANS was supported by the Heising-Simons Foundation (2020–1911). We thank Mathieu Morlighem for support in setting up the ISSM Greenland domain.

675 References

- 676 Andrews, L. C., Catania, G. A., Hoffman, M. J., Gulley, J. D., Lüthi, M. P., Ryser, C., ... Neumann, T. A. (2014, Oct 01). Direct observations of evolving subglacial drainage beneath the Greenland Ice Sheet. *Nature*, *514*(7520), 80–83. doi: 10.1038/nature13796
- 680 Aschwanden, A., Fahnestock, M. A., Truffer, M., Brinkerhoff, D. J., Hock, R., Khroulev, C., ... Khan, S. A. (2019). Contribution of the Greenland Ice Sheet to sea level over the next millennium. *Science advances*, *5*(6), eaav9396.

- 683 Bartholomew, I., Nienow, P., Sole, A., Mair, D., Cowton, T., Palmer, S., & Wad-
684 ham, J. (2011). Supraglacial forcing of subglacial drainage in the ablation
685 zone of the Greenland ice sheet. *Geophysical Research Letters*, *38*(8). doi:
686 <https://doi.org/10.1029/2011GL047063>
- 687 Brinkerhoff, D. J., Aschwanden, A., & Fahnestock, M. (2021). Constraining
688 subglacial processes from surface velocity observations using surrogate-
689 based bayesian inference. *Journal of Glaciology*, *67*(263), 385–403. doi:
690 10.1017/jog.2020.112
- 691 Brinkerhoff, D. J., Meyer, C. R., Bueler, E., Truffer, M., & Bartholomew, T. C.
692 (2016). Inversion of a glacier hydrology model. *Annals of Glaciology*, *57*(72),
693 84–95. doi: 10.1017/aog.2016.3
- 694 Cornford, S. L., Martin, D. F., Lee, V., Payne, A. J., & Ng, E. G. (2016). Adaptive
695 mesh refinement versus subgrid friction interpolation in simulations of Antarc-
696 tic ice dynamics. *Annals of Glaciology*, *57*(73), 1–9. doi: 10.1017/aog.2016.13
- 697 de Fleurian, B., Werder, M. A., Beyer, S., Brinkerhoff, D. J., Delaney, I., Dow,
698 C. F., ... et al. (2018). SHMIP The subglacial hydrology model inter-
699 comparison Project. *Journal of Glaciology*, *64*(248), 897–916. doi:
700 10.1017/jog.2018.78
- 701 Felden, A. M., Martin, D. F., & Ng, E. G. (2023). SUHMO: an adaptive mesh re-
702 finement subglacial hydrology model v1.0. *Geoscientific Model Development*,
703 *16*(1), 407–425. doi: 10.5194/gmd-16-407-2023
- 704 Flowers, G. E. (2015). Modelling water flow under glaciers and ice sheets. *Proceed-*
705 *ings of the Royal Society A: Mathematical, Physical and Engineering Sciences*,
706 *471*(2176), 20140907.
- 707 Hager, A. O., Hoffman, M. J., Price, S. F., & Schroeder, D. M. (2022). Persist-
708 ent, extensive channelized drainage modeled beneath Thwaites Glacier, West
709 Antarctica. *The Cryosphere*, *16*(9), 3575–3599. doi: 10.5194/tc-16-3575-2022
- 710 Helanow, C., Iverson, N. R., Woodard, J. B., & Zoet, L. K. (2021). A slip law for
711 hard-bedded glaciers derived from observed bed topography. *Science Advances*,
712 *7*(20), eabe7798. doi: 10.1126/sciadv.abe7798
- 713 Hewitt, D. R., Chini, G. P., & Neufeld, J. A. (2018). The influence of a poroelas-
714 tic till on rapid subglacial flooding and cavity formation. *Journal of Fluid Me-*
715 *chanics*, *855*, 1170–1207. doi: 10.1017/jfm.2018.624
- 716 Hewitt, I. J. (2009). *Mathematical modelling of geophysical melt drainage* (PhD the-
717 sis). University of Oxford.
- 718 Hewitt, I. J. (2011). Modelling distributed and channelized subglacial drainage: the
719 spacing of channels. *Journal of Glaciology*, *57*(202), 302–314. doi: 10.3189/
720 002214311796405951
- 721 Hewitt, I. J. (2013). Seasonal changes in ice sheet motion due to melt water lubri-
722 cation. *Earth and Planetary Science Letters*, *371-372*, 16–25. doi: [https://doi](https://doi.org/10.1016/j.epsl.2013.04.022)
723 [.org/10.1016/j.epsl.2013.04.022](https://doi.org/10.1016/j.epsl.2013.04.022)
- 724 Joughin, I., Smith, B. E., & Howat, I. M. (2018). A complete map of greenland ice
725 velocity derived from satellite data collected over 20 years. *Journal of Glaciol-*
726 *ogy*, *64*(243), 1–11. doi: 10.1017/jog.2017.73
- 727 Kyrke-Smith, T. M., Katz, R. F., & Fowler, A. C. (2014). Subglacial hydrology and
728 the formation of ice streams. *Proceedings of the Royal Society A: Mathemat-*
729 *ical, Physical and Engineering Sciences*, *470*(2161), 20130494. doi: 10.1098/
730 rspa.2013.0494
- 731 MacGregor, J. A., Fahnestock, M. A., Catania, G. A., Aschwanden, A., Clow, G. D.,
732 Colgan, W. T., ... Seroussi, H. (2016). A synthesis of the basal thermal state
733 of the Greenland Ice Sheet. *Journal of Geophysical Research: Earth Surface*,
734 *121*(7), 1328–1350. doi: <https://doi.org/10.1002/2015JF003803>
- 735 Maier, N., Humphrey, N., Harper, J., & Meierbachtol, T. (2019). Sliding dominates
736 slow-flowing margin regions, Greenland Ice Sheet. *Science Advances*, *5*(7),
737 eaaw5406. doi: 10.1126/sciadv.aaw5406

- 738 Moon, T., Joughin, I., Smith, B., van den Broeke, M. R., van de Berg, W. J.,
739 Noël, B., & Usher, M. (2014). Distinct patterns of seasonal Greenland
740 glacier velocity. *Geophysical Research Letters*, *41*(20), 7209–7216. doi:
741 <https://doi.org/10.1002/2014GL061836>
- 742 Morlighem, M., Rignot, E., Seroussi, H., Larour, E., Ben Dhia, H., & Aubry, D.
743 (2010). Spatial patterns of basal drag inferred using control methods from a
744 full-stokes and simpler models for pine island glacier, west antarctica. *Geophys-*
745 *ical Research Letters*, *37*(14). doi: <https://doi.org/10.1029/2010GL043853>
- 746 Morlighem, M., Williams, C. N., Rignot, E., An, L., Arndt, J. E., Bamber, J. L., ...
747 Zinglensen, K. B. (2017). Bedmachine v3: Complete bed topography and ocean
748 bathymetry mapping of greenland from multibeam echo sounding combined
749 with mass conservation. *Geophysical Research Letters*, *44*(21), 11,051–11,061.
750 doi: <https://doi.org/10.1002/2017GL074954>
- 751 Mouginot, J., Rignot, E., Bjørk, A. A., Van den Broeke, M., Millan, R., Morlighem,
752 M., ... Wood, M. (2019). Forty-six years of Greenland Ice Sheet mass balance
753 from 1972 to 2018. *Proceedings of the national academy of sciences*, *116*(19),
754 9239–9244.
- 755 Nienow, P. W., Sole, A. J., Slater, D. A., & Cowton, T. R. (2017, Dec 01). Recent
756 Advances in Our Understanding of the Role of Meltwater in the Greenland
757 Ice Sheet System. *Current Climate Change Reports*, *3*(4), 330–344. doi:
758 [10.1007/s40641-017-0083-9](https://doi.org/10.1007/s40641-017-0083-9)
- 759 Otosaka, I., Shepherd, A., Ivins, E., Schlegel, N., Amory, C., van den Broeke, M., ...
760 others (2023). *Mass balance of the Greenland and Antarctic ice sheets from*
761 *1992 to 2020. Earth Syst Sci Data 15 (4): 1597-1616.*
- 762 Poinar, K. (2023). Seasonal flow types of glaciers in sermilik fjord, greenland,
763 over 2016–2021. *Journal of Geophysical Research: Earth Surface*, *128*(7),
764 e2022JF006901. doi: <https://doi.org/10.1029/2022JF006901>
- 765 Poinar, K., Dow, C. F., & Andrews, L. C. (2019). Long-Term Support of an Ac-
766 tive Subglacial Hydrologic System in Southeast Greenland by Firn Aquifers.
767 *Geophysical Research Letters*, *46*(9), 4772–4781. doi: [https://doi.org/10.1029/](https://doi.org/10.1029/2019GL082786)
768 [2019GL082786](https://doi.org/10.1029/2019GL082786)
- 769 Popinet, S. (2013–2024). *Basilisk*. <http://basilisk.fr>.
- 770 Rada, C., & Schoof, C. (2018). Channelized, distributed, and disconnected: sub-
771 glacial drainage under a valley glacier in the Yukon. *The Cryosphere*, *12*(8),
772 2609–2636. doi: [10.5194/tc-12-2609-2018](https://doi.org/10.5194/tc-12-2609-2018)
- 773 Rignot, E., & Mouginot, J. (2012). Ice flow in Greenland for the International Polar
774 Year 2008–2009. *Geophysical Research Letters*, *39*(11). doi: [https://doi.org/10](https://doi.org/10.1029/2012GL051634)
775 [.1029/2012GL051634](https://doi.org/10.1029/2012GL051634)
- 776 Schoof, C. (2005). The effect of cavitation on glacier sliding. *Proceedings of the*
777 *Royal Society A: Mathematical, Physical and Engineering Sciences*, *461*(2055),
778 609–627. doi: [10.1098/rspa.2004.1350](https://doi.org/10.1098/rspa.2004.1350)
- 779 Schoof, C. (2010). Ice-sheet acceleration driven by melt supply variability. *Nature*,
780 *468*(7325), 803–806. doi: [10.1038/nature09618](https://doi.org/10.1038/nature09618)
- 781 Schoof, C. (2023). The evolution of isolated cavities and hydraulic connection at
782 the glacier bed. Part 1: steady states and friction laws. *EGUsphere*, *2023*, 1–
783 27. doi: [10.5194/egusphere-2022-1380](https://doi.org/10.5194/egusphere-2022-1380)
- 784 Seroussi, H., Morlighem, M., Rignot, E., Khazendar, A., Larour, E., & Mouginot,
785 J. (2013). Dependence of century-scale projections of the greenland ice
786 sheet on its thermal regime. *Journal of Glaciology*, *59*(218), 1024–1034. doi:
787 [10.3189/2013JoG13J054](https://doi.org/10.3189/2013JoG13J054)
- 788 Shapero, D. R., Joughin, I. R., Poinar, K., Morlighem, M., & Gillet-Chaulet, F.
789 (2016). Basal resistance for three of the largest greenland outlet glaciers.
790 *Journal of Geophysical Research: Earth Surface*, *121*(1), 168–180. doi:
791 <https://doi.org/10.1002/2015JF003643>
- 792 Sommers, A., Meyer, C., Morlighem, M., Rajaram, H., Poinar, K., Chu, W., &

- 793 Meija, J. (2023). Subglacial hydrology modeling predicts high winter water
794 pressure and spatially variable transmissivity at Helheim Glacier, Greenland.
795 *Journal of Glaciology*, 1–13. doi: 10.1017/jog.2023.39
- 796 Sommers, A., Rajaram, H., & Morlighem, M. (2018). SHAKTI: subglacial hydrology
797 and kinetic, transient interactions v1.0. *Geoscientific Model Development*,
798 *11*(7), 2955–2974. doi: 10.5194/gmd-11-2955-2018
- 799 Vijay, S., King, M. D., Howat, I. M., Solgaard, A. M., Khan, S. A., & Noël, B.
800 (2021). Greenland ice-sheet wide glacier classification based on two distinct
801 seasonal ice velocity behaviors. *Journal of Glaciology*, *67*(266), 1241–1248. doi:
802 10.1017/jog.2021.89
- 803 Walder, J. S. (1982). Stability of sheet flow of water beneath temperate glaciers and
804 implications for glacier surging. *Journal of Glaciology*, *28*(99), 273–293.
- 805 Warburton, K. L. P., Hewitt, D. R., & Neufeld, J. A. (2023). Shear dilation of sub-
806 glacial till results in time-dependent sliding laws. *Proceedings of the Royal*
807 *Society A: Mathematical, Physical and Engineering Sciences*, *479*(2269),
808 20220536. doi: 10.1098/rspa.2022.0536
- 809 Werder, M. A., Hewitt, I. J., Schoof, C. G., & Flowers, G. E. (2013). Modeling chan-
810 nnelized and distributed subglacial drainage in two dimensions. *Journal of Geo-*
811 *physical Research: Earth Surface*, *118*(4), 2140–2158. doi: [https://doi.org/10](https://doi.org/10.1002/jgrf.20146)
812 [.1002/jgrf.20146](https://doi.org/10.1002/jgrf.20146)
- 813 Zimmerman, R. W., Al-Yaarubi, A., Pain, C. C., & Grattoni, C. A. (2004).
814 Non-linear regimes of fluid flow in rock fractures. *International Journal*
815 *of Rock Mechanics and Mining Sciences*, *41*, 163–169. (Proceedings of
816 the ISRM SINOROCK 2004 Symposium) doi: [https://doi.org/10.1016/](https://doi.org/10.1016/j.ijrmms.2004.03.036)
817 [j.ijrmms.2004.03.036](https://doi.org/10.1016/j.ijrmms.2004.03.036)
- 818 Zwally, H. J., Abdalati, W., Herring, T., Larson, K., Saba, J., & Steffen, K. (2002).
819 Surface Melt-Induced Acceleration of Greenland Ice-Sheet Flow. *Science*,
820 *297*(5579), 218–222. doi: 10.1126/science.1072708